Progress in Natural Science: Materials International 31 (2021) 420–427

HOSTED BY

Contents lists available at ScienceDirect

Progress in Natural Science: Materials International

journal homepage: www.elsevier.com/locate/pnsmi

Original Research

Structure and effect of diamagnetism on manganese lithium phosphate glass to cathode materials application

Pichitchai Butnoi [a], Wipada Senanon [a], Narong Chanlek [a], Yingyot Poo-arporn [a], Supree Pinitsoontorn [b], Santi Maensiri [c,d,e], Prayoon Songsiriritthigul [c,d], Pongtanawat Khemthong [c,f], Pinit Kidkhunthod [a,c,e,*]

[a] Synchrotron Light Research Institute (Public Organization), 111 University Avenue, Muang District, Nakhon Ratchasima, 30000, Thailand
[b] Insitute of Nanomaterials Research and Innovation for Energy (IN-RIE), Khon Kaen University, Khon Kaen, 40002, Thailand
[c] Research Network NANOTEC-SUT on Advanced Nanomaterials and Characterization, School of Physics, Institute of Science, Suranaree University of Technology, Nakhon Ratchasima, 30000, Thailand
[d] School of Physics, Institute of Science, Suranaree University of Technology, Nakhon Ratchasima, 30000, Thailand
[e] Center of Excellent on Advanced Functional Materials, Suranaree University of Technology, Nakhon Ratchasima, 30000, Thailand
[f] National Nanotechnology Center, National Science and Technology Development Agency, Pathumthani, 12120, Thailand

ARTICLE INFO

Keywords:
XAS
XANES
EXAFS
Manganese lithium phosphate glass
Diamagnetism

ABSTRACT

1-x(Li_2O–$2P_2O_5$)-$x$$MnO_2$ glasses where x = 0.2, 0.3 and 0.4 mol%, respectively, were synthesized by melted-quenching method. The Mn and P oxidation states and local structures around Mn and P-ions including Mn–O and P–O bonding distances and coordination numbers have been studied via X-ray absorption near edge structure (XANES) and extended X-ray absorption fine structure (EXAFS), respectively. XANES results exhibit a coexistence of oxidation state of Mn^{2+} and Mn^{3+} with a mean value of 2.82. Moreover, Mn and P *K*-edge EXAFS show the Mn–O and P–O bonding distances of approximately 2.083–2.094 Å and 1.766–1.774 Å, respectively. A paramagnetism was found for all Mn–P glasses. Additionally, the coercive field (H_c) and remnant magnetization (M_r) increased with increasing Mn contents. However, the low specific capacitances are seriously obtained (<40 F g^{-1}) suggesting the effect of natural diamagnetism of lithium phosphate based-glass unlike the borate based-glasses which originally exhibit paramagnetism.

1. Introduction

Generally, glasses are common use as in photonic and optical materials applications. Particular, its low-cost production, easy to form into desired shape and fast fabrication. Thus, various research works on glasses have been focusing on developing optical properties of glasses by doping with various rare earth ions into the glass networks [1,2]. The glass former is very importance parameter for glasses preparation. The famous glasses former such as B_2O_3, SiO_2, P_2O_5 has been reported by many previous reported [2–5]. Phosphate glass is one of an interesting glass former due to its low melting temperature, high transparency, and high solubility [2,6]. Moreover, phosphate glass has specific properties including high thermal conductivity and high thermal expansion coefficient [7]. Lithium phosphate-based materials with crystal phase is widely reported in lithium-ions batteries in term of electrode materials especially cathode [8,9] because of its good electrochemical performances, long cycling life, high voltage, light weight [10,11]. However, based on our knowledge, lithium-ion battery or super capacitor devices revealed that the safety issues especially flammable and swollen occurs from liquid electrolyte or degradable of metal oxide during charge-discharge mechanism. Thus, glasses or glass ceramics have been investigated because they have better thermal expansion than polymer composite materials. Nevertheless, the performance of glass-based electrodes are not good enough because glass has low ionic and electric conductivity. Many researchers have been paid attention to overcome the limited of glass by combined different ions in glass matrix such as V^{4+}, P^{5+}, Li^{+}, *etc*. Recently, the phosphate-based glass has been reported as high-voltage cathodes for magnesium and lithium batteries. For example, Arthur et al. [12] reported that amorphous V_2O_5–P_2O_5 exhibits high capacity and voltage due to the multiple oxidation states of V^{2+} to V^{5+}. Thus, the oxidation state of glass transition metal in glass structure can play an important key to an improvement for energy storage application of

* Corresponding author.
E-mail address: pinit@slri.or.th (P. Kidkhunthod).

https://doi.org/10.1016/j.pnsc.2021.03.004
Received 7 April 2020; Received in revised form 15 March 2021; Accepted 31 March 2021
Available online 2 May 2021

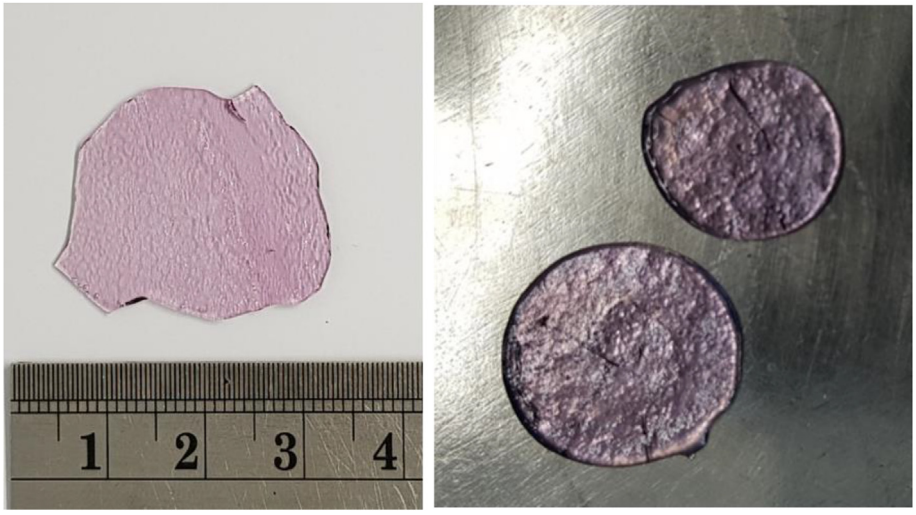

Fig. 1. Photograph of the prepared glass samples.

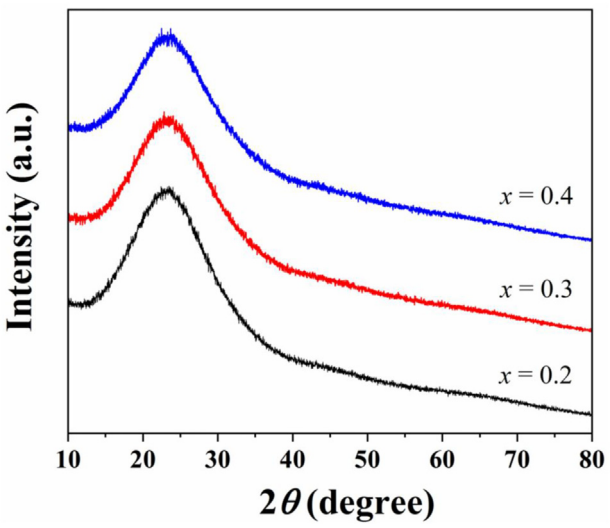

Fig. 2. X-ray diffraction patterns of 1-x(Li_2O–$2P_2O_5$) - $x$$MnO_2$ glass samples: x = 0.2, 0.3 and 0.4.

glasses. Manganese is one of the most abundant elements of the earth, good environment friendly and inexpensive materials. Moreover, manganese oxides can exhibit various Mn oxidation states which is interesting for electrode materials. Additionally, manganese oxide has been widely studied and synthesized in various compound forms by different methods for use as electrode materials of energy storage devices such as battery and supercapacitor.

Synchrotron-based x-ray absorption spectroscopy (XAS) is one of the most useful analytical techniques not only for crystalline materials but also for amorphous materials [13,14]. Generally, the XAS technique can be used to characterize the short-range order and the long-range order for determining the local structure around selected atom which different XRD technique, its request long-range crystalline order. Thus, XAS technique has been widely used to analyze the structural of crystal, amorphous or glass in many research fields [15,16].

In this work, we reported the local structure information, optical, and magnetic properties of 1-x(Li_2O–$2P_2O_5$) - xMnO_2 glasses with x = 0.2, 0.3, and 0.4 (mol%) prepared by melt-quenching method. The native various structure and phase formation of the glass samples were characterized by X-ray diffraction (XRD) technique. Scanning electron microscopy (SEM) and energy dispersive spectroscopy (EDS) were analyzed the morphologies and the element distribution, respectively. In addition, Transmission electron microscopy (TEM) analysis was used to confirm the glassy state of the prepared glass samples. Furthermore, the

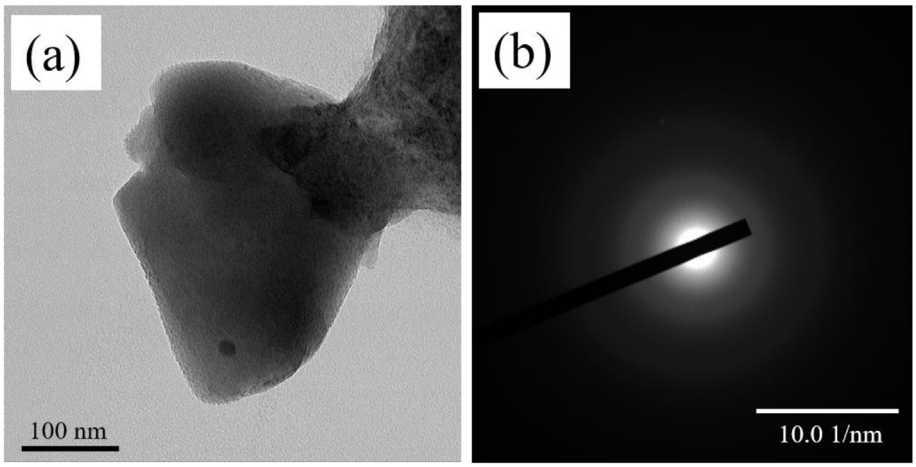

Fig. 3. TEM image and selected area electron diffraction pattern of some selected glassy samples.

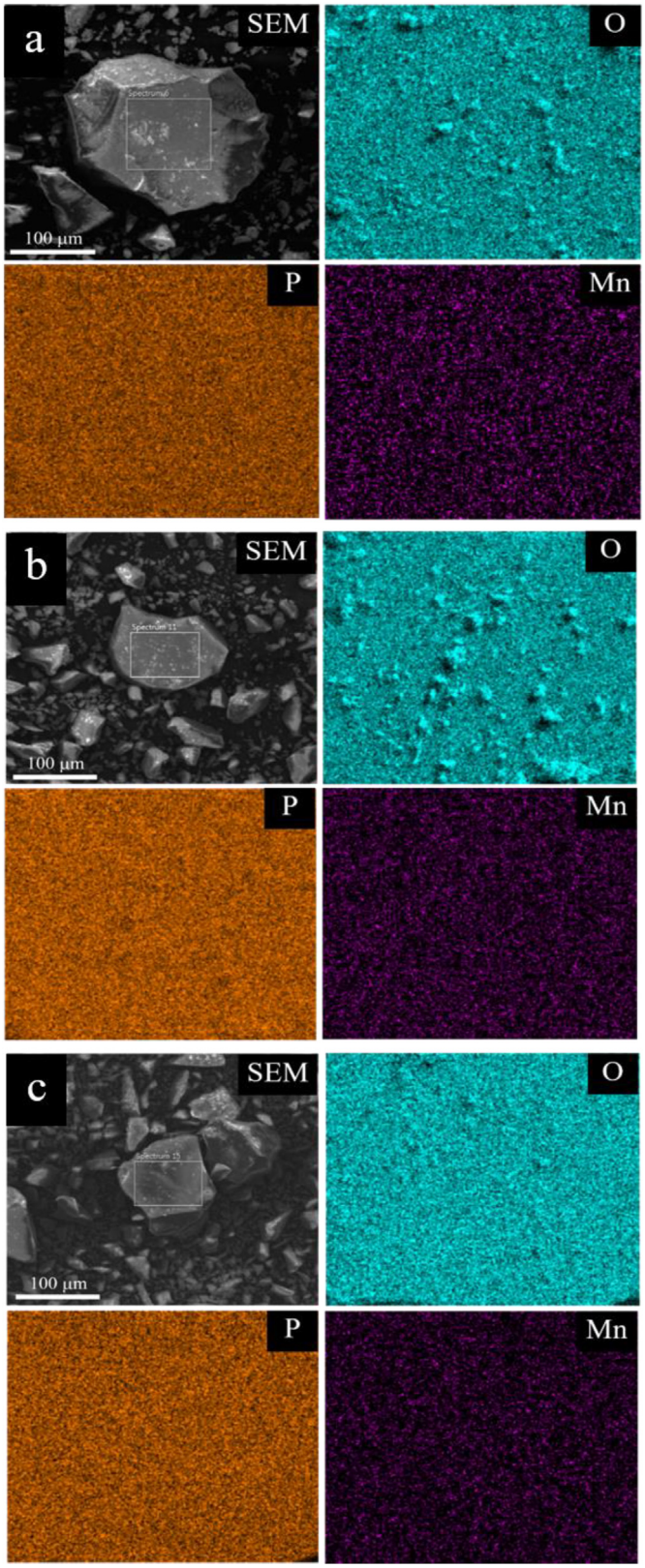

Fig. 4. SEM images and EDS spectrum for the selected region and its corresponding EDS mapping images of 1-x(Li_2O–$2P_2O_5$) - $x$$MnO_2$ glass samples: (a) x = 0.2, (b) x = 0.3 and (c) x = 0.4.

synchrotron-based X-ray absorption spectroscopy (XAS) technique and X-ray photoelectron spectroscopy (XPS) has been used to deeply understand a structure-function of the glass samples, a local structure information around Mn-ions and P-ions including bonding distance, coordination number, oxidation states. Moreover, ultraviolet–visible spectroscopy (UV–Vis) and vibrating sample magnetometer (VSM) were used for the optical and magnetic properties Measurements. Additionally, the electrochemical properties of these prepared glassed also measured in order to investigate the possibility of these glasses as energy storage materials.

2. Experimental method

2.1. Glass preparation

Manganese lithium phosphate glasses with chemical system 1-x(Li_2O–$2P_2O_5$) - $x$$MnO_2$ where x = 0.2, 0.3 and 0.4 mol% were fabricated from high purity of starting materials of lithium carbonate (Li_2CO_3, 99.5%, Himedia), Phosphorus pentoxide (P_2O_5, 99.99%, Sigma-Aldrich) and Manganese dioxide (MnO_2, 99%, Himedia) mixed in stoichiometric amounts of powder. The 1-x(Li_2O–$2P_2O_5$) - $x$$MnO_2$ glasses were prepared by the conventional melt quenching technique including of two-step processes. Firstly, the compound of Li_2CO_3 and P_2O_5 powders were weight and mixed in stoichiometric amounts Li_2O–$2P_2O_5$ in an agate mortar and melted in alumina crucible at 1100. °C for 1 h in an electrical furnace. After the molten completely, the melted was rapidly poured out on stainless-steel plate and pressed quickly with another plate at room temperature (RT). The Li_2O–$2P_2O_5$ glass sample was grounded to fine powders. Batches of (1-x)Li_2O–$2P_2O_5$-$x$$MnO_2$ powders were mixed and melted in alumina crucible at 1200 °C for 30 min in an electrical furnace and quenched at RT similar first step. The transparent glass with violet color was fabricated by this part as shown in Fig. 1.

2.2. Characterization

The phase formation of glass samples was confirmed by using X-ray diffraction (XRD) technique, performed on Rigaku SmartLab with a Cu (λ of $Cu_{K\alpha}$ = 1.542 Å) source. All XRD data were collected in the range of 2 theta between 10 and 80° at room temperature. The morphologies and the element distribution of the prepared glass samples were identified by scanning electron microscopy (SEM) and energy dispersive spectroscopy (EDS) (FEI quanta 450), respectively. Moreover, the microstructure of glass powder was observed using a transmission electron microscopy (TEM; Tecnai G^2 20 S-TWIN). In addition, the elements information of the glass particle surface was detected by an X-ray photoelectron spectroscopy (XPS) technique using a PHI 5000 with Probe II XPS system and the K-alpha X-rays of aluminum (Al K-alpha E = 1.487 keV) source. The XPS measurements were performed at BL. 5.3 at SLRI Thailand.

Synchrotron-based X-ray absorption spectra (XAS) technique including X-ray absorption near edge structure (XANES) and X-ray absorption fine structure (EXAFS) spectra were collected Mn and P K-edges in transmission mode at the SUT-NANOTEC-SLRI XAS beamline 5.2, SLRI, Thailand. The local structure and the valence state information of Mn and P atoms will be obtained from XAS [14–17].

The optical and magnetic properties of glass samples were measured at room temperature using the UV–Vis–NIR spectroscopy (PerkinElmer-Lambda 950 spectrophotometer) in the range of 200–800 nm and a vibrating sample magnetometer (VSM) option in the Quantum Design Versalab instrument with the applied magnetic field range of ±10 kOe, respectively.

The electrochemical property of obtained glasses were studied in 1 M KOH electrolyte by potentiostate/galvanostat (Metrohm autolab) which consist of three electrode configuration, Ag/AgCl, Platinum wire (Pt) and the obtained glass samples as counter, reference and active electrode. The electrode preparation was composed of 80% by weight of prepared glass samples, 10% by weight of polyvinylideneflouoride (PVDF) binder and 10% by weight of carbon black. The compounds were mixed in inside an agent mortar with N-methyl-2-pyrrolidinone. The obtained slurry was dropped on nickel foam substrate and dried at 80 °C in an oven. The

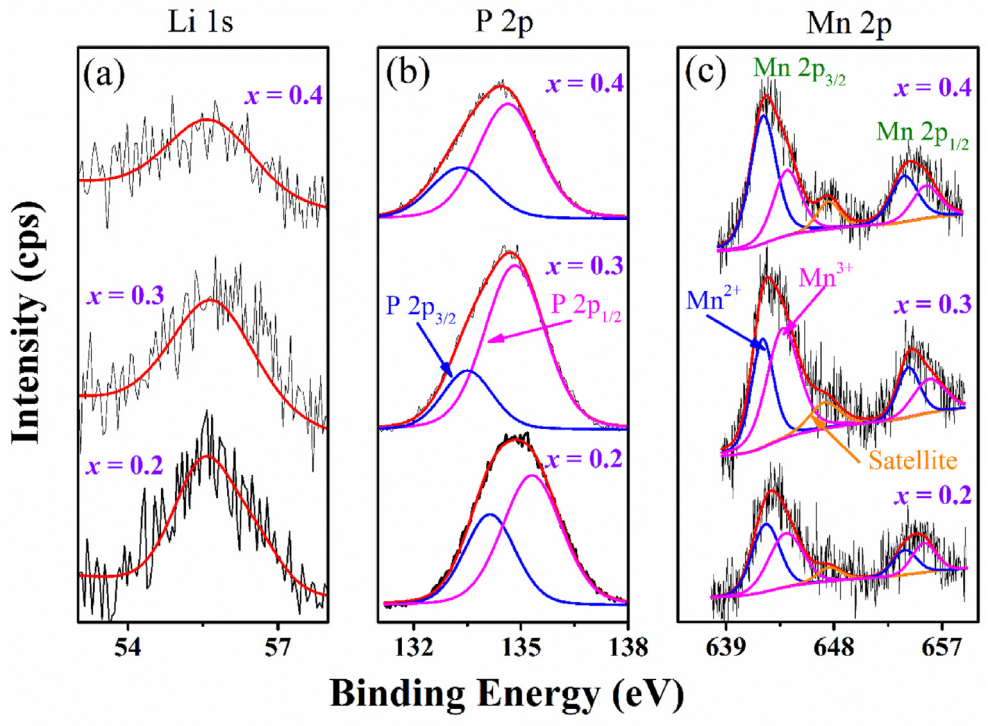

Fig. 5. XPS spectra of (a) Lithium, (b) Phosphorus and (c) Manganese of 1-x(Li_2O–$2P_2O_5$) - $x$$MnO_2$ glass samples: x = 0.2, 0.3 and 0.4.

cyclic voltammetry (CV) measuring were performed in a potential window between −1.25 V and 0.55 V at different scan rates of 5, 10, 50, 100, 150 and 200 mVs^{-1}, respectively.

3. Results and discussion

The XRD patterns of 1-x(Li_2O–$2P_2O_5$) - $x$$MnO_2$ glasses powder were illustrated in Fig. 2. The patterns present the nature pattern of amorphous phase, no detectable Bragg's peaks. In addition, the broad peaks around 15–30° presented the diffused scattering signal arising from disordered structures in the material [18,19]. This behavior confirmed purely amorphous phase with a short-range structure or disordering structure of prepared glass samples. Moreover, Transmission Electron Microscopy (TEM) technique was also carried out to confirm the amorphous phase of the fabricated glass samples. Bright field TEM image and selected area electron diffraction pattern of some selected samples is presented in Fig. 3. The diffraction spot exhibits diffusion spot, indicating the nonappearance of any crystalline phase in prepared glasses. This confirms a purely glassy and amorphous structures [20]. According to the electron diffraction patterns, no available any reflection was observed. It can be confirmed that the prepared glass is homogeneity of amorphous (glass) materials.

Fig. 4(a–c) illustrate the selected SEM region and EDS mapping of oxygen (O), phosphorus (P) and manganese (Mn) elements of 1-x(Li_2O–$2P_2O_5$) - $x$$MnO_2$ glasses powder. The EDS mapping confirmed the presence of O, P and Mn elements in glass samples. In addition, the mapping area revealed the homogeneous distribution of each element, suggesting that the elements were dispersed in the prepared glasses which displayed in different colors dot. Generally, EDS technique can be used to provide the elemental composition information in term of qualitative elements, however detection of the small atomic number element e.g. Li cannot be achieved by this technique. This because lithium element is a light element, in which it has low energy level that they struggle to escape from the sample without being absorbed.

In order to further investigate the trace elements and the oxidation states of atoms on surface of 1-x(Li_2O–$2P_2O_5$) - $x$$MnO_2$ glass samples. X-

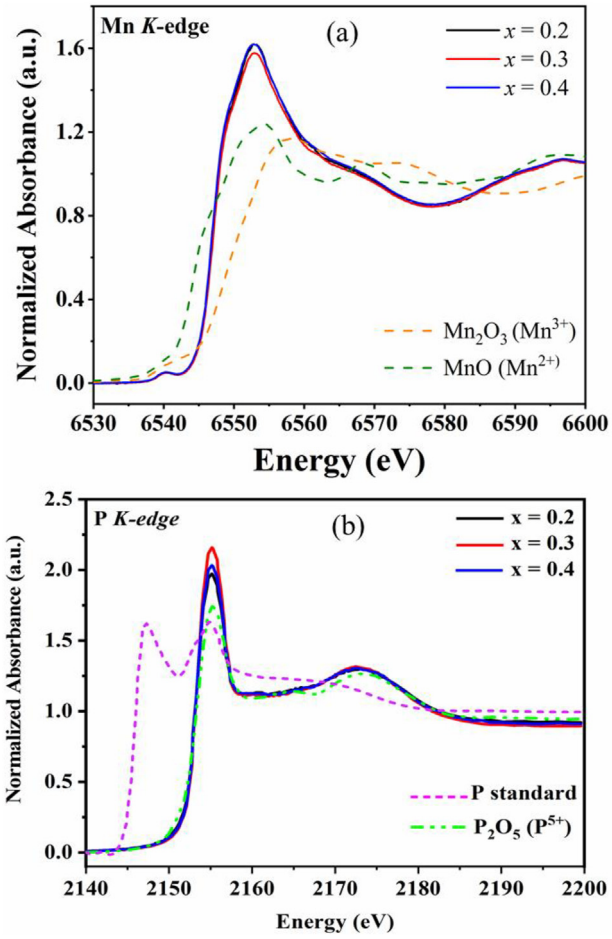

Fig. 6. XANES spectra of 1-x(Li_2O–$2P_2O_5$) - $x$$MnO_2$ glass samples and standard samples: (a) Mn K-edge and (b) P K-edge: x = 0.2, 0.3 and 0.4.

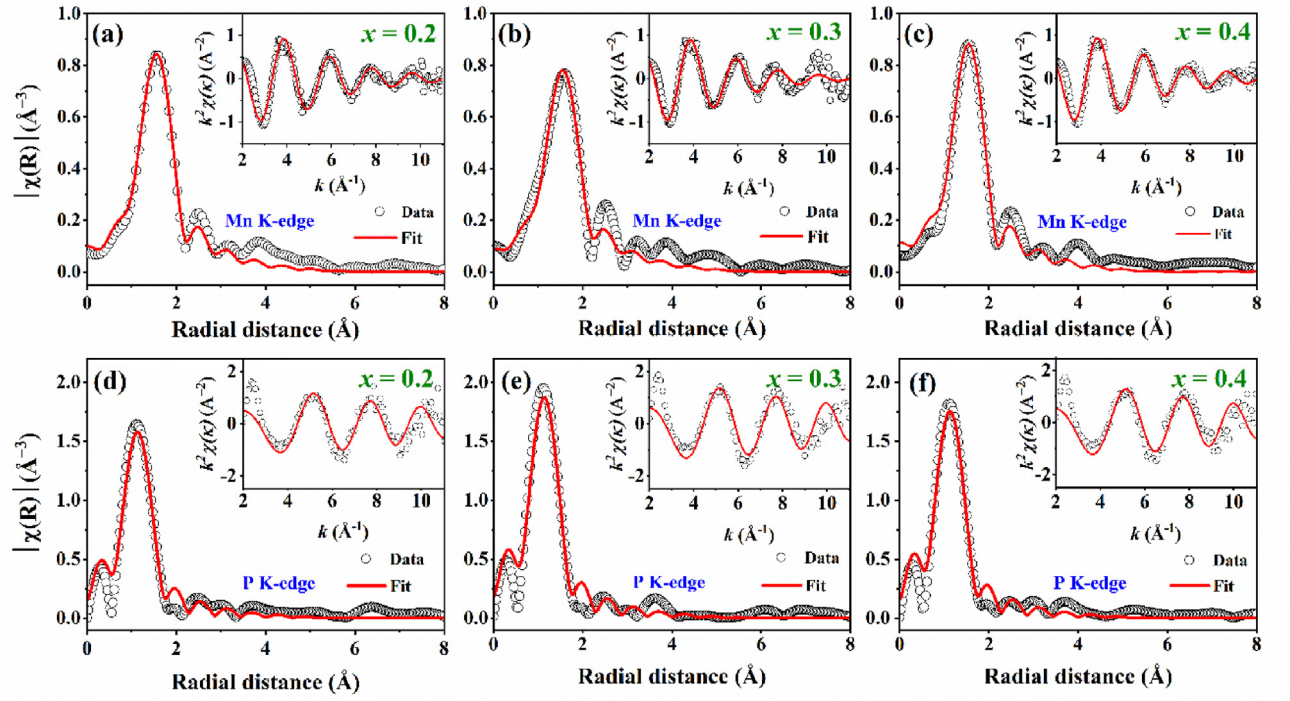

Fig. 7. Experimental and simulated EXAFS spectrum of Fourier transformed (FT) of Mn *K*-edge (inset: $k^2\chi(k)$ EXAFS spectra) of 1-*x*(Li_2O–$2P_2O_5$) - *x*MnO_2 glass samples: Mn K-edge (a) $x = 0.2$, (b) $x = 0.3$, (c) $x = 0.4$ and P K-edge (d) $x = 0.2$, (e) = 0.3 and (c) = 0.4.

Table 1
EXAFS fitting parameters including coordination numbers (N), amplitude reduction (S_0^2), Debye–Waller factors (σ), interatomic distances (R) and R-factor of 1-*x*(Li_2O–$2P_2O_5$) - *x*MnO_2 glass samples.

Samples	Paths	*N*	σ^2	E_0 (eV)	R (Å)	R-factor
$x = 0.2$	Mn–O	3.747	0.00796	−2.103	2.09345	0.006
	P–O	5.693	0.00202	−5.039	1.77139	0.027
$x = 0.3$	Mn–O	3.942	0.01014	−2.061	2.09433	0.027
	P–O	6.641	0.00190	−4.272	1.77414	0.026
$x = 0.4$	Mn–O	3.675	0.00666	−3.309	2.08281	0.006
	P–O	6.272	0.00194	−5.904	1.76664	0.025

ray photoelectron spectroscopy (XPS) measurement was performed as shown in Fig. 5(a–c). Moreover, XPS technique can be used to confirm the presence of Li elements in this glass. The binding energy of carbon (C 1s) was used to calibrate of all spectra. The binding energies of Li 1s, P 2p, Mn $2p_{3/2}$ and Mn $2p_{1/2}$ are approximately 56, 135, 641 and 653 eV, respectively [21]. The high-resolution spectra of P 2p in Fig. 5(b) can be fitted into two major peaks, P $2p_{3/2}$ and P $2p_{1/2}$ at about 134.13 and 135.31 eV. In addition, The Mn 2p spectrum has two main peaks as displayed in Fig. 5(c), Mn $2p_{3/2}$ and Mn $2p_{1/2}$ of Mn^{2+} and Mn^{3+}, respectively. The Mn 2p3/2 can be fitted into 2 peaks of Mn^{2+} and Mn^{3+} at 641.8 and 643.3 eV. This indicates that the mixing of Mn^{2+} and Mn^{3+} in glass samples.

Fig. 6(a–b) shows normalized XANES spectra at Mn and P *K*-edge of all samples compared with MnO (Mn^{2+}) and Mn_2O_3 (Mn^{3+}) standard samples. At Mn K-edge, it was found that the positions of the absorption edge of all the samples lied between absorption edge of Mn^{2+} and Mn^{3+} standard samples. This indicated a present of a coexistent of oxidation state of Mn^{2+} and Mn^{3+} in all various samples [22,23]. Moving to K-edge, it can be noticed no shift of absorption edge for each sample with increasing of MnO_2 contents was observed. Additionally, the similar feature of P–K-edge XANES spectra was also observed. These suggest P atom in all samples have the same oxidation number with four-fold oxygen coordination network around P atoms [24–26]. In detail, the difference of white line intensities of P *K*-edge XANES spectra are clearly observed which responds to the number of oxygen atoms around phosphorus atoms in glass structure. The high white line intensity, the large number of oxygen coordinated network around P atoms. This will be feature discussed in the EXAFS fitting section.

In order to study the local environment around Mn and P atoms in the obtained glass samples, X-ray absorption fine structure (EXAFS) spectra of the glass structure were carefully analyzed and fitted. Their Fourier transform in R space (k = 3–10 $Å^{-1}$) with $k^2\chi$ (k) EXAFS spectra as set and the first shell fitting was determined for Mn–O (Mn K-edge) and P–O (P K-edge) bonding distance, respectively, as shown in Fig. 7(a–f). The best EXAFS fitting parameters were already obtained with the reasonable and acceptable parameters [27] including interatomic distances (R), coordination numbers (N) and Debye–Waller factors (σ^2) and R factor for quality to the fit are shown in Table 1. The Mn–O and P–O bonding distances were obtained approximately 2.082–2.094 Å and 1.767–1.771, respectively. With increasing Mn contents, the interatomic distance of Mn–O and P–O slightly increase.

The study of optical absorption is useful to understand optical transition and electronic structure of the glasses. The UV–Vis absorption spectra of different concentrations for MnO_2 doped with glass systems in the wavelength range of 200–800 nm is displayed in Fig. 8. The positions of absorption peak show three main absorption regions at 200–250 nm, 250–400 nm and 400–800 nm, respectively. It can be seen that the intensity of absorbance peak decrease with increasing Mn contents suggesting the increasing of Mn contents can affect the light absorption behavior of the glass samples. Thus, the UV–Vis absorption regions around 200–250 nm in this work are presented the charge transfer of $O^{2-} \rightarrow Mn^{2+}$ [28,29] and the charge transfer of $O^{2-} \rightarrow Mn^{3+}$ at 250–400 nm [30]. In addition, the d–d crystal field transitions on octahedral Mn^{3+} species [30,31] are identified as 400–460 nm [31]. From the UV–Vis results, the mixing of Mn^{2+} and Mn^{3+} oxidation states are observed which is consistent with the previous result obtained from XANES and XPS studies.

To determine the band gap (E_g) from the absorbance spectra of the prepared glasses. The Tauc-plot method was used, the E_g can be determined by extrapolating the linear region of plots $\alpha h\upsilon^{1/2}$ versus photon

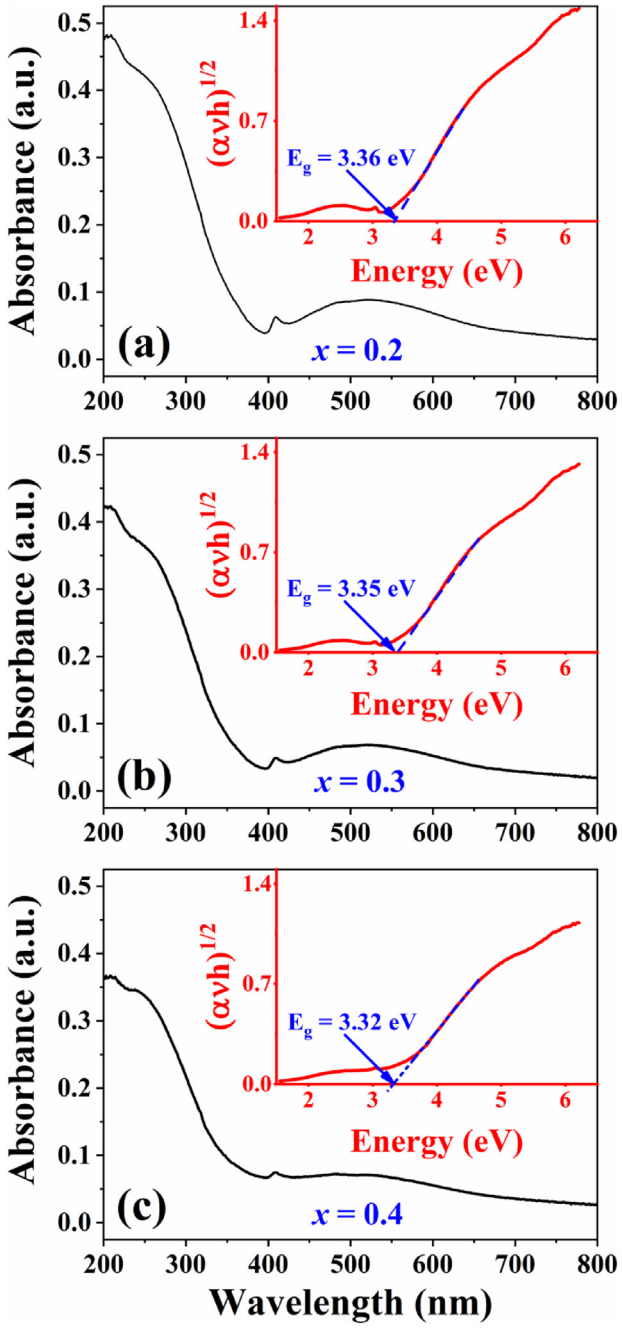

Fig. 8. Optical absorbance spectra of 1-x(Li_2O–$2P_2O_5$) - $x$$MnO_2$ glasses (inset: plot of $(\alpha h\nu)^{1/2}$ versus energy for showing the optical band gap): (a) $x = 0.2$, (b) $x = 0.3$ and (c) $x = 0.4$.

energy (hυ) with calculated using the following equation [22,23,32,33].

$$\alpha h\upsilon = A(h\upsilon - E_g)^2 \quad (1)$$

where E_g is the optical band gap energy for indirect band gap, A is constant, α is the absorption coefficient, hυ is the photon energy. These plots are presented in inset of Fig. 8. The calculated E_g of the obtained glass were found to be decreased with increasing of Mn contents. The decrease of E_g with Mn contents increase might affect to the magnetic properties of glasses. This will be discussed in the next section.

The magnetization curves of 1-x(Li_2O–$2P_2O_5$) - $x$$MnO_2$ glass samples measured at room temperature with an applied magnetic field between −10 kOe and 10 kOe are presented in Fig. 9. For the M − H loop of Li_2O–$2P_2O$ based-glass is also shown inset in Fig. 9, in which diamagnetic

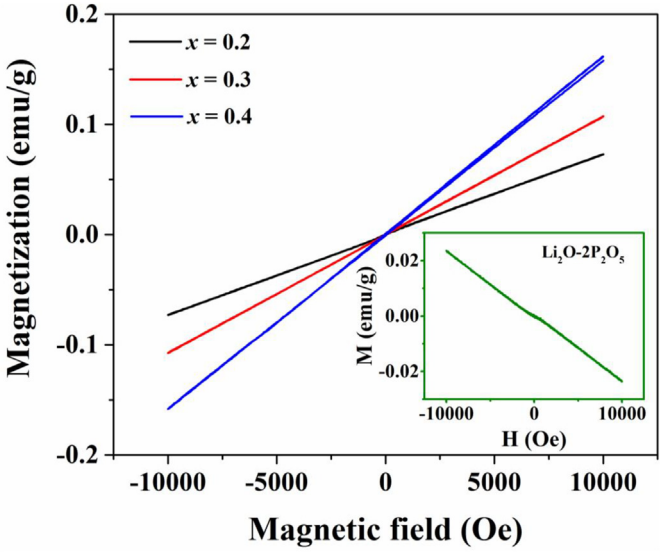

Fig. 9. Magnetization (M) as a function of the magnetic field (H) curves of 1-x(Li_2O–$2P_2O_5$) - $x$$MnO_2$ glass samples with $x = 0.2$, 0.3 and 0.4 (inset; Plot of M versus H of Li_2O–$2P_2O_5$ glass).

behavior was clearly observed. However, the increasing of Mn contents lead to significantly transform of the diamagnetism to paramagnetic behavior. This is because manganese oxides are generally paramagnetism. Furthermore, due to the different unpaired electron per Mn atom, Mn ions in glasses are presented in various Mn oxidation states resulting to different magnetic properties [34,35]. The M − H loops of prepared glass samples presents a paramagnetic behavior which the M − H loops show linearly line when applied magnetic field to sample. It can be noticed that the increasing of MnO_2 contents affect to an increase the maximum magnetization. In contrast, the coercive field (H_c) and remnant magnetization (M_r) increased with increasing MnO_2 contents.

Fig. 10 exhibited the cyclic voltammograms (CV) of manganese lithium phosphate glass systems of a) 0.2(Li_2O–$2P_2O_5$) – 0.8MnO_2, b) 0.3(Li_2O–$2P_2O_5$) – 0.7MnO_2 and c) 0.4(Li_2O–$2P_2O_5$) – 0.6MnO_2 glasses at different scan rates from 10 mVs^{-1} to 200 mVs^{-1} in 1 M KOH electrolyte. The capacitive behaviour of all glass samples shown a pair redox peaks which consist of charging process (oxidation) with whole range from 0.39 to 0.49 V and discharging process (reduction) with whole range from 0.285 to 0.31 V. The peaks current slightly shifted with high scan rates which ascribed to resistance of the electrode [36]. The specific capacitance of cyclic voltammograms (C_{CV}) measurement of the glass electrodes were calculated follow by equation below.

$$C_{CV} = \frac{1}{vm\Delta V}\int IdV \quad (2)$$

where ν is the scan rates (mVs^{-1}), m is the active mass of materials (g), ΔV is the potential window (V) and I is response current (A).

The calculated specific capacitance of 1-x(Li_2O–$2P_2O_5$) - $x$$MnO_2$ at x = 0.2, 0.3 and 0.4 mol% glass systems from the area of CV curve at difference scan rates of 5, 10, 50, 100, 150 and 200 mVs^{-1} trend to decrease with increasing scan rates. From this study, it was found that the calculated specific capacitances were obtained between 15 and 36 F g^{-1}. In addition, at x = 0.4, the maximum specific capacitance was obtained approximately 36 F g^{-1} with the lowest scan rate of 5 mVs^{-1}. The low specific capacitances obtained in this study might come from the natural diamanetism of phosphate based-glass unlike the reported study of borate based-glasses which originally exhibit paramegnetism [37].

4. Conclusions

In this work, the 1-x(Li_2O–$2P_2O_5$) - $x$$MnO_2$ glass systems have been

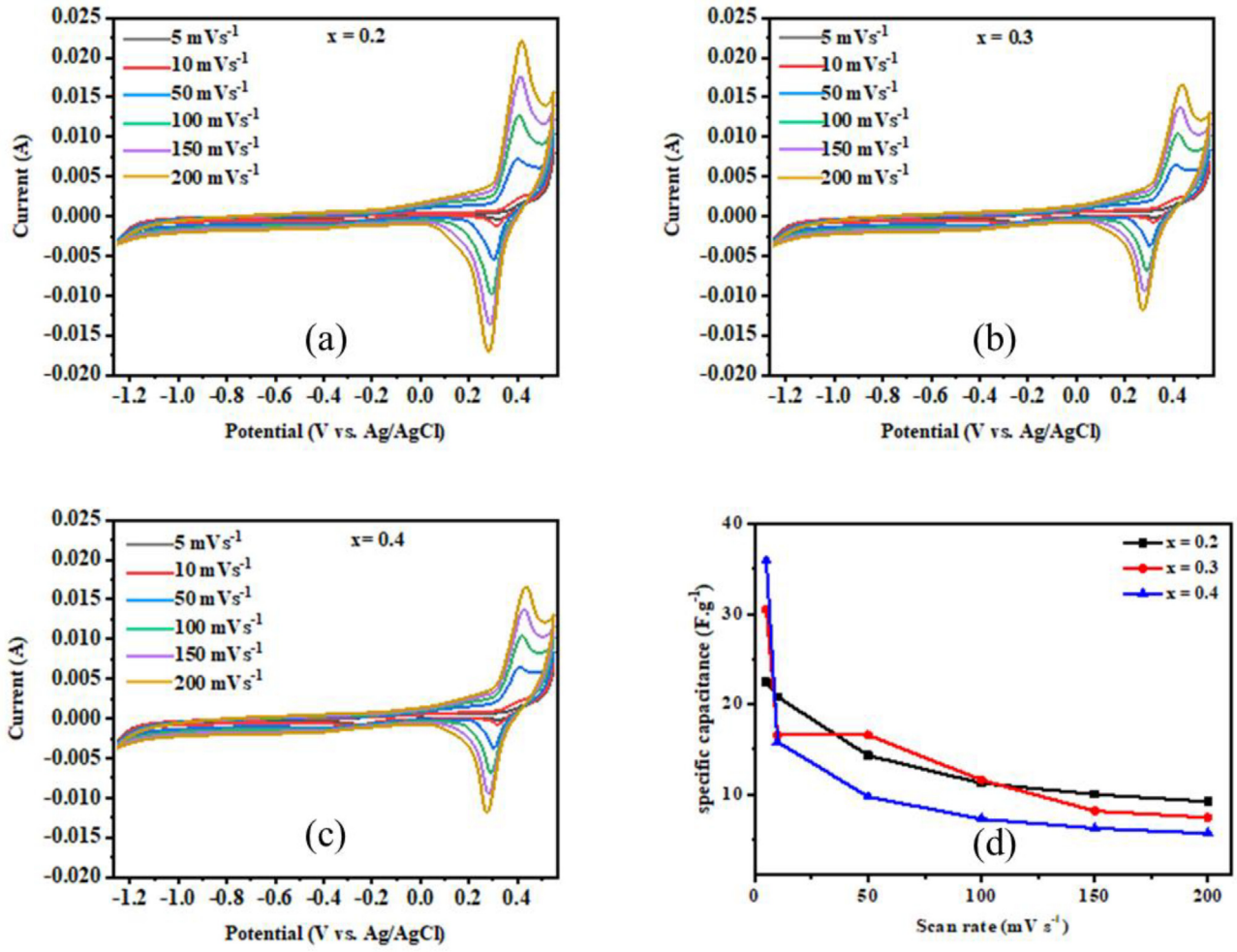

Fig. 10. Cyclic voltammograms of (a) 0.2(Li_2O–$2P_2O_5$) – 0.8MnO_2, (b) 0.3(Li_2O–$2P_2O_5$) –. 0.7MnO_2, (c) 0.4(Li_2O–$2P_2O_5$) – 0.6MnO_2 glasses at different scan rates and (d) plot of specific capacitance versus scan rates.

synthesized via melt-quenching method. All XRD patterns present broad and no detectable peaks which confirmed purely amorphous phase. The UV–Vis and XAS analysis confirmed the mixed oxidation state of $Mn^{2+/}Mn^{3+\cdot}$ The mixed oxidation state of $Mn^{2+/}Mn^{3+}$corresponding to Mn K-edge results were measured by advanced synchrotron-based X-ray absorption near edge structure (XANES). From EXAFS study, the average Mn–O and P–O bonding distance were found in the range of 2.082–2.094 Å and 1.767–1.771 Å, respectively. The magnetic properties of Li_2O–$2P_2O_5$ show diamagnetic behaviour. However, the diamagnetic behaviour transformed to paramagnetic behaviour when increasing Mn contents. The electrochemical of electrode materials were studied with 1 M of KOH electrolyte. The obtained specific capacitance is quite low which exhibits diamanetism of phosphate-based glass, which is not suitable to be used as energy storage applications.

Declaration of competing interest

I do declare there is no conflict of interest of this manuscript.

Acknowledgments

The authors thank financial support from the Synchrotron Light Research Institute (Public Organization), the authors are also grateful to the SUT-NANOTEC-SLRI XAS beamline (BL5.2), Thailand for the XAS experiment. Thanks to Research network NANOTEC-SUT on Advanced Nanomaterials and characterization for financial support. The authors also thank to Department of Physics, Khon Kaen University for VSM facilities and School of Physics and Center of Excellent on Advanced Functional Materials (CoE-AFM), Suranaree University of Technology for laboratory facilities supported.

References

[1] F. Lahoz, C. Perez-Rodriguez, S.E. Hernandez, I.R. Martin, V. Lavin, U.R. Rodriguez-Mendoza, Sol. Energy Mater. Sol. Cells 95 (2011) 1671–1677.
[2] N. Chanthima, N. Kiwsakunkran, J. Kaewkhao, N. Sangwaranatee, Journal of Metals, Materials and Minerals 29 (2) (2019) 58–63.
[3] T. Hashimoto, H. Inukai, K. Matsumura, H. Nasu, A. Ishihara, Y. Nishio, Sensor. Actuator. B Chem. 257 (2018) 807–814.
[4] S. Banerjee, A.K. Tyagi, Functional Materials: Preparation, Processing and Applications, Elsevier, Inc., London, 2012.
[5] M.H.A. Mhareb, S. Hashim, S.K. Ghoshal, Y.S.M. Alajerami, M.A. Saleh, R.S. Dawaud, N.A.B. Razak, S.A.B. Azizan, Opt. Mater. 37 (2014) 391–397.
[6] A.A. Ahmed, A.A. Ali, A. El-Fiqi, The Journal of Materials Research and Technology 8 (1) (2019) 1003–1013.
[7] M.R. Sahar, B. Astuti, M.S. Rohani, Opt. Rev. 13 (2) (2006) 101–103.
[8] Y. Li, W.Q. Bai, Y.D. Zhang, X.Q. Niu, D.H. Wang, X.L. Wang, C.D. Gu, J.P. Tu, J. Power Sources 282 (2015) 100–108.
[9] J. Zhu, W. Li, F. Chenga, A. Lu, J. Mater. Chem. 3 (2015) 13920–13925.
[10] J. Barker, M. Saidi, J. Swoyer, Electrochemical, Solid State Letters 6 (2003) A53–A55.
[11] S. Karthikprabhu, K. Karuppasamy, D. Vikraman, K. Prasanna, T. Maiyalagan, A. Nichelson, A. Kathalingam, H. Kim, Appl. Surf. Sci. 449 (2018) 435–444.
[12] T.S. Arthur, K. Kato, J. Germain, J. Guo, P. Glans, Y. Liu, D. Holmes, X. Fan, F. Mizuno, Chem. Commun. 51 (2015) 15657–15660.

[13] M. West, A.T. Ellis, P.J. Potts, C. Streli, C. Vanhoof, D. Wegrzynek, P. Wobrauschek, J. Anal. At. Spectrom. 26 (2011) 1919–1963.
[14] P. Kidkhunthod, Adv. Nat. Sci. Nanosci. Nanotechnol. 8 (2017), 035007.
[15] N. Laorodphan, P. Kidkhunthod, J. Khajonrit, A. Montreeuppathum, N. Chanlek, S. Pinitsoontorn, S. Maensiri, J. Non-Cryst. Solids 497 (2018) 56–62.
[16] A. Madheshiya, C. Gautam, S. Kumar, Journal of Asian Ceramic Societies 5 (2017) 276–283.
[17] W. Klysubun, P. Kidkhunthod, P. Tarawarakarn, P. Sombunchoo, C. Kongmark, S. Limpijumnong, S. Rujirawat, R. Yimnirun, G. Tumcharern, K. Faungnawakij, J. Synchrotron Radiat. 24 (2017) 707–716.
[18] T.R. Welberry, D.J. Goossens, Acta Crystallogr. A: Foundations and Advances 64 (1) (2008) 23–32, https://doi.org/10.1107/S0108767307041918.
[19] T.R. Welberry, D.J. Goossens, IUCrJ 1 (6) (2014) 550–562, https://doi.org/10.1107/S205225251402065X.
[20] J. Kasl, Š. Mikmeková, S.E.M. D Jandová, Mater. Sci. Eng. 55 (2014), 012008. https://www.globalsino.com/EM/.
[21] J. Zheng, L. Ni, Y. Lu, C. Qin, P. Liu, T. Wu, Y. Tang, Y. Chen, J. Power Sources 282 (2015) 444–451.
[22] P. Butnoi, N. Chanlek, Y. Poo-arporn, S. Pinitsoontorn, S. Maensiri, P. Kidkhunthod, J. Alloys Compd. 809 (2019) 151811.
[23] J. Khajonrit, A. Montreeuppathum, P. Kidkhunthod, N. Chanlek, Y. Poo-arporn, S. Pinitsoontorn, S. Maensiri, J. Alloys Compd. 763 (2018) 199–208.
[24] A. Ziletti, A. Carvalho, P.E. Trevisanutto, D.K. Campbell, D. F. Coker, A.H. Castro Neto, Phys. Rev. B Vol. 91 pp. 085407-1-085407-9 2015.
[25] E.H. Arbib, B. Elouadi, J.P. Chaminade, J. Darriet, J. Solid State Chem. 127 (1996) 350–353.
[26] A. Redeker, G. Kuper, J. Hormes, F. Frick, M. Janen, M. Muhlhauser, vol. 76, Gordon and Breach Science Publishers S.A., 1993, pp. 239–242.
[27] P.G. Bruce, et al., Nat. Mater. 11 (2012) 19–29.
[28] V.C. Bose, V. Biju, Phys. E Low-dimens. Syst. Nanostruct. 66 (2015) 24–32.
[29] X. Hao, J. Zhao, Y. Li, Y. Zhao, D. Ma, L. Li, Colloid. Surface. Physicochem. Eng. Aspect. 374 (2011) 42–47.
[30] J.B. Macstre, E.F. López, J. Gallardo-Amores, R.R. Casero, V.S. Escribano, E.P. Bernal, Int. J. Inorg. Mater. 3 (2001) 889–899.
[31] Z. Jin, H. Ma, G. Li, Y. Xu, G. Ma, Z. Cheng, Appl. Phys. Lett. 100 (2012), 021106.
[32] C. Dayanand, R. Sarma, G. Bhikshamaiah, M. Salagram, J. Non-Cryst. Solids 167 (1994) 122–126.
[33] G. Vijayaprasath, R. Murugan, S. Palanisamy, N.M. Prabhu, T. Mahalingam, Y. Hayakawa, G. Ravi, Mater. Res. Bull. 76 (2016) 48–61.
[34] S. Yoon, S.H. Kang, S. Lee, K. Kim, J.P. Song, M. Kim, Y.K. Kwon, Phys. Chem. Chem. Phys. 29 (2019) 15932–15939.
[35] S. Zhang, D. Zhao, Advances in Magnetic Materials Processing, Properties, and Performance, CRC Press, 2017.
[36] Y.G. Wang, H.Q. Li, Y.Y. Xia, Adv. Mat. 18 (2006) 2619–2623.
[37] P. Butnoi, N. Chanlek, Y. Poo-arporn, S. Pinitsoontorn, S. Maensiri, P. Kidkhunthod, J. Alloys Compd. Vol. 809, pp. 151811-1-151811-9.